

Normalize Filters! Classical Wisdom for Deep Vision

Gustavo Perez¹

Stella X. Yu^{1,2}

¹Electrical Engineering and Computer Sciences, University of California, Berkeley

²Computer Science and Engineering, University of Michigan

{gperezs, stellayu}@berkeley.edu, stellayu@umich.edu

Abstract

Classical image filters, such as those for averaging or differencing, are carefully normalized to ensure consistency, interpretability, and to avoid artifacts like intensity shifts, halos, or ringing. In contrast, convolutional filters learned end-to-end in deep networks lack such constraints. Although they may resemble wavelets and blob/edge detectors, they are not normalized in the same or any way. Consequently, when images undergo atmospheric transfer, their responses become distorted, leading to incorrect outcomes. We address this limitation by proposing filter normalization, followed by learnable scaling and shifting, akin to batch normalization. This simple yet effective modification ensures that the filters are atmosphere-equivariant, enabling co-domain symmetry. By integrating classical filtering principles into deep learning (applicable to both convolutional neural networks and convolution-dependent vision transformers), our method achieves significant improvements on artificial and natural intensity variation benchmarks. Our ResNet34 could even outperform CLIP by a large margin. Our analysis reveals that unnormalized filters degrade performance, whereas filter normalization regularizes learning, promotes diversity, and improves robustness and generalization.

1 Introduction

Image filtering is a cornerstone of classical computer vision; averaging and differencing filters play a fundamental role in noise reduction, edge detection, and feature extraction. These filters are meticulously designed and normalized to ensure consistent and interpretable results (Fig. 1).

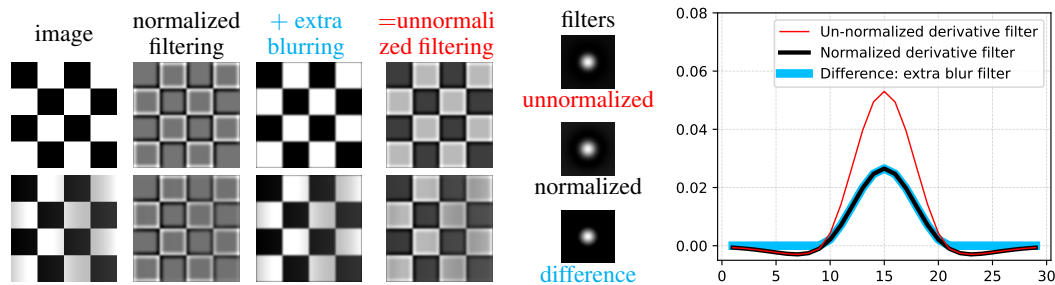


Figure 1: **Filter normalization is critical in classical computer vision for consistency and interpretability, while unnormalized filters obtained by deep learning lack this property.** **Left:** For a checkerboard (Column 1) under uniform (Row 1) and varied (Row 2) illumination, we compare responses from normalized (Column 2) and unnormalized (Column 4) filters; the latter equals the sum of the former and extra blurring (Column 3). **Right:** For normalized and unnormalized Difference-of-Gaussian (DoG) filters, we show their horizontal profiles at the center row and their difference. Normalized DoG detects edges despite illumination changes, while unnormalized DoG introduces blurring that varies with illumination, overpowering edges with mean response shifts.

Filter normalization is critical because it prevents artifacts such as intensity shifts, halos, and ringing, which can distort the output and undermine the reliability of downstream tasks. For example, in Gaussian blurring, the filter kernel is normalized so that its weights sum to 1, preserving the overall intensity of the image while smoothing out fine details. Similarly, Gaussian derivative filters are normalized so that its positive weights sum to +1 and negative weights sum to -1, enabling accurate edge detection and allowing edge strengths to be compared across different types of derivative filters. This careful normalization process has been a hallmark of classical filtering, ensuring consistency and robustness across a wide range of applications (See Fig. 1).

In contrast, convolutional filters in deep networks are not explicitly designed but are instead learned end-to-end, emerging through an optimization process driven by data and training loss. While these filters may resemble wavelets, blob detectors, or edge detectors [41, 24, 29, 40, 32, 18], they are not normalized in the same - or any - way as their classical counterparts. This lack of normalization can lead to unpredictable behavior, particularly when the input data deviates from the training distribution.

In Fig. 1, for the checkerboard under uniform and uneven illumination, the normalized Difference of Gaussian (DoG) filter consistently detects checker edges. In contrast, the unnormalized DoG filter, whose positive weights sum to +2 and negative weights to -1, is equivalent to the sum of the normalized DoG and a normalized blur filter. This extra blurring causes the response to shift with illumination and overwhelm the edge response of the normalized DoG.

Such illumination effects, commonly found in autonomous driving, medical imaging, and remote sensing, can be modeled as Atmospheric Transfer Functions (ATFs) [2], which linearly map the physical reflectance of a scene to the luminance in the image. Varying the gain and bias of the linear map simulates real-world effects like brighter/dimmer/hazy scenes (See Fig. 2). However, the responses of unnormalized filters to such intensity changes can become distorted, compromising the neural network’s performance.

Data augmentation and instance normalization [33] are two common methods to address data distribution shifts. However, the former requires anticipating domain shifts in advance and increases training complexity, while the latter assumes that all pixels in an image follow the same statistics and cannot handle spatially varying biases, e.g., Fig. 1.

We propose *filter normalization*, a novel approach that normalizes convolutional filters followed by learnable scaling and shifting, akin to batch normalization. This simple yet effective modification ensures that the filters are atmosphere-equivariant, with consistent responses under varying conditions.

Our extensive experiments on artificial and natural intensity variation benchmarks demonstrate that our approach is not only robust but also outperforms larger models of ResNet [13] and Vision Transformer (ViT) [10] architectures. Most strikingly, ResNet34 with feature normalization surpasses CLIP, the

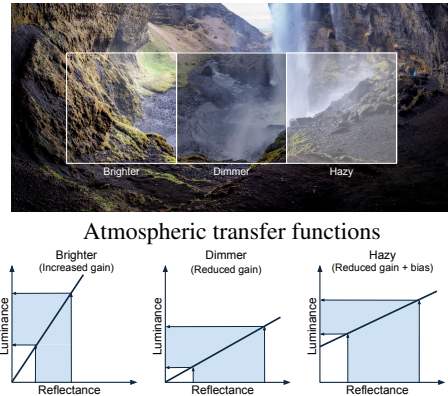


Figure 2: **The same visual scene can be seen very differently under various atmospheric conditions.** Lighting, shadows, and haze can be modeled by Atmospheric Transfer Functions (ATFs) [2], which map the physical reflectance of a scene to the luminance in the image. Varying gains and biases can simulate effects like brighter/dimmer/hazy scenes.

behavior, particularly when the input data

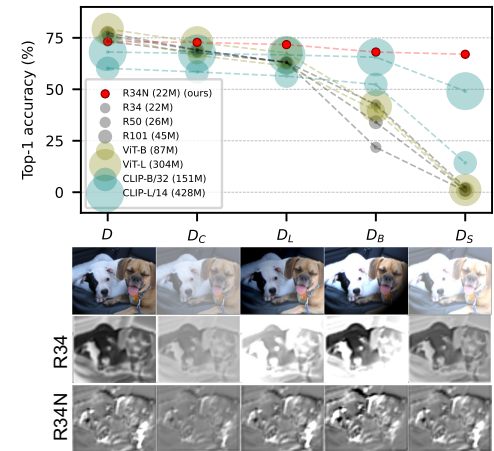


Figure 3: **Feature normalization outperforms larger ResNet and ViT models, including CLIP, in accuracy and robustness on atmospheric transfer benchmarks.** Every model is trained on D , the original ImageNet dataset, but tested on D and its four ATF variations: D_C, D_L, D_B, D_S , as illustrated for the image example in Row 1. The response of a ResNet34 filter with filter normalization (Row 3) remains more robust and informative than the one without normalization (Row 2) to such intensity transformation.

extensively trained large vision-language model, by an absolute 20% on ImageNet in hazy conditions (Fig. 3). Consistent gains are observed on ImageNet, ExDark, and LEGUS benchmarks. Our analysis further reveals that unnormalized filters degrade performance, whereas filter normalization regularizes learning and promotes diversity, leading to better robustness and generalization.

Our contributions. **1)** Identifies unnormalized filters as a key limitation in deep learning, distorting responses under intensity variations. **2)** Proposes *filter normalization* with learnable scaling/shifting, ensuring *atmosphere equivariance*. **3)** Achieves consistent gains across CNNs and ViTs on intensity variation benchmarks, outperforming larger models, including CLIP. **4)** Enhances robustness and generalization through diverse, interpretable filters.

2 Related work

Deep networks’ performance can be severely impacted by atmospheric transformations. To mitigate this, various approaches have been developed such as architecture modifications to achieve equivariance to some transformations, normalization layers to enhance network robustness to instance-level perturbations, and data augmentations to improve robustness and generalization.

Equivariance and invariance to transformations. Several works have proposed modifications to deep neural networks to achieve equivariance or invariance to specific transformations. For instance, [5, 22, 19] introduced model modifications to achieve equivariance to rotations, [36] used circular harmonics to achieve equivariance to rotation and translation, [11] achieved invariance to translation and equivariance to rotation and scale, while [23, 15] focus on image denoising.

Complex-valued deep learning has also been studied to achieve codomain symmetry to geometric and color transformations [30]. [4] is another approach that achieves equivariance through transformations on a scaling and rotation manifold. To the best of our knowledge, other than [15, 6], existing methods focus on geometric transformations and overlook atmospheric variations like gain-bias shifts. Closest to our work, [15] proposes equivariant networks to gain and bias. However, our proposed normalization also provides practical invariance to bias, leading to improved robustness.

Normalization layers. Instance Normalization (IN) [33] layers can be added to the network to reduce instance-specific biases, improving robustness to multiplicative and additive effects. However, IN may not fully address covariate shift, leading to suboptimal training. On the other hand, batch normalization (BN) [16] layers reduce covariate shift, but fail to address instance-specific biases. Other normalization techniques, such as group normalization (GN) [38], which balances the benefits of BN and IN by dividing channels into groups, have also been proposed. However, these methods operate on feature activations, whereas our approach introduces a data-agnostic modification to the convolutional layer by normalizing filter weights. This allows our method to address instance-specific biases while still enabling training with BN to handle covariate shift, resulting in improved training.

Data augmentation. Atmospheric effects are frequently addressed with data augmentations, which are a common technique for improving model robustness. Automated augmentation strategies like RandAugment [8] and AutoAugment [7] have been proposed to reduce the search space of data perturbations. However, they increase training complexity and require prior knowledge of the target domain since it is challenging to account for all possible variations in the deployment data. In contrast, our approach provides inherent robustness to these perturbations, eliminating the need for extensive data augmentation.

Deep network architectures. CNN architectures such as ResNets [13] have been successful due to their ability to capture spatial hierarchies and local correlations. ViTs [10], on the other hand, employ an attention-based mechanism that allows for global interactions between image regions, enabling more flexible and context-dependent feature extraction. However, more recent architectures like ConvNeXt [20] have demonstrated comparable performance to ViTs, while maintaining the efficiency and interpretability of traditional CNNs. Other approaches like Convolutional Vision Transformer (CvT) [37] improve ViTs by adding convolutions. Our approach can be applied to any convolution-based architecture, and we show that leaner models with our normalized convolutions outperform large attention-based models like CLIP [26] in robustness to atmospheric corruptions.

3 Filter normalization for deep learning

We have shown that unnormalized filters obtained by deep learning lack consistency and interpretability with respect to atmospheric transfer functions (Fig. 1). We will first relate an arbitrary filter

to normalized filters followed by scaling and shifting. We then prove atmosphere equivariance of normalized filters.

3.1 Any filter is both averaging and differencing

We connect a convolutional filter with weights w to classical averaging (blur) and differencing (derivative) filters. The filter response, y , to k inputs x_1, \dots, x_k , is defined as:

$$y = f(x; w) = \sum_{i=1}^k w_i x_i. \quad (1)$$

We divide w into positive and negative parts. Let $1(\cdot)$ denote the indicator function which outputs 1 if the input is positive and 0 otherwise. Let \circ denote the Hadamard product (multiplication of elements). We have:

$$w = w^+ - w^- \quad (2)$$

$$w^+ = w \circ 1(w > 0) \quad (3)$$

$$w^- = (-w) \circ 1(w < 0) \quad (4)$$

where both w^+ and w^- are nonnegative $k \times 1$ vectors. The L_1 norm $\|\cdot\|_1$ of these vectors is simply the total sum of their respective weights. We will use L_1 norm exclusively throughout this paper, with $\|\cdot\|_1$ as $\|\cdot\|$ for short.

We define the *positive weight ratio* of a filter, denoted by r , as the ratio between the algebraic sum and the total absolute sum of all the weights (See Fig. 4). We have:

$$r(w) = \frac{\sum_{i=1}^k w_i}{\sum_{i=1}^k |w_i|} = \frac{\|w^+\| - \|w^-\|}{\|w^+\| + \|w^-\|} \quad (5)$$

$$\sum_{i=1}^k w_i = \|w^+\| - \|w^-\| = \|w\| \cdot r(w). \quad (6)$$

It is straightforward to prove the following properties.

1. $|r(w)| \leq 1$.
2. $r(w) = 1$ (-1) when and only when all non-zero weights of w are positive (negative).
3. $r(w) \gtrless 0$ when and only when $\|w^+\| \gtrless \|w^-\|$.

In classical computer vision, there are two types of filters: averaging and differencing filters, each type normalized properly to ensure consistency and interpretability:

$$\text{averaging: } \|w^+\| = 1, \|w^-\| = 0, r(w) = 1 \quad (7)$$

$$\text{differencing: } \|w^+\| = 1, \|w^-\| = 1, r(w) = 0 \quad (8)$$

That is, an averaging filter produces a normalized weighted average of its inputs, and a differencing filter produces the difference between two normalized weighted sums, one using positive weights and the other negative weights.

We show that an unnormalized filter w is a weighted sum of a differencing filter and an averaging filter (Fig. 1). Without loss of generality, we assume $\|w^+\| \geq \|w^-\|$; otherwise, we can study $-w$ instead. We have:

$$w = w^+ - w^- = \|w^-\| \cdot \underbrace{\left(\frac{w^+}{\|w^+\|} - \frac{w^-}{\|w^-\|} \right)}_{\text{differencing filter}} + (\|w^+\| - \|w^-\|) \cdot \underbrace{\frac{w^+}{\|w^+\|}}_{\text{averaging filter}}. \quad (9)$$

Therefore, a general filter behaves between averaging and differencing, and the closer its positive weight ratio is to 0 (1), the more dominant differencing (averaging) it becomes.

3.2 Filter normalization

Consider the input intensity x modulated by a scalar gain factor g and a scalar offset o :

$$x \rightarrow g \cdot x + o. \quad (10)$$

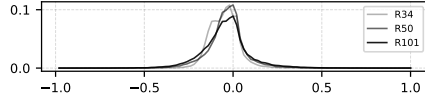


Figure 4: **Convolutional filters learned in CNNs are unnormalized, leaning more toward differencing than averaging.** The distribution of the *positive weight ratio* of filters for each model optimized for ImageNet classification is skewed towards 0, indicating that most filters primarily perform differencing.

If $g > 1$ ($g < 1$), the image looks brighter (dimmer) with an expanded (reduced) range; if $g < 1$ and $o > 0$, the image looks brighter and hazy with reduced contrast (Fig. 2). For any unnormalized filter w , the response becomes

$$f(g \cdot x + o) = g \cdot f(x) + o \cdot \|w\| \cdot r(w) = \begin{cases} g \cdot f(x) + o, & \text{if } w \text{ is averaging} \\ g \cdot f(x), & \text{if } w \text{ is differencing} \end{cases} \quad (11)$$

That is, normalized filters produce consistent and interpretable responses with respect to intensity changes: Both averaging and differencing filters are equivariant to intensity gain modulation and shifts; in particular, differencing filters are invariant to intensity shifts.

If all filters in a layer are normalized, their responses are scaled uniformly by the same gain factor g . For unnormalized filters, however, their responses will be scaled differently, each by the filter’s total weight sum, $\|w\|r(w)$, thereby altering the feature representation at that layer.

We address this limitation by proposing filter normalization, followed by learnable scaling and shifting, akin to batch normalization. A convolutional filter of kernel size k in deep learning is parametrized by weight w and scalar offset b . Given an arbitrary filter w , we first normalize its positive and negative parts individually:

$$y = \sum_{i=1}^k w_i x_i + b = \|w\| \sum_{i=1}^k \frac{w_i}{\|w\|} x_i + b = \|w\| \sum_{i=1}^k \left(\frac{w_i^+}{\|w\|} - \frac{w_i^-}{\|w\|} \right) x_i + b \quad (12)$$

$$\rightarrow \underbrace{a}_{\text{scaling}} \sum_{i=1}^k \underbrace{\left(\frac{w_i^+}{\|w^+\| + \varepsilon} - \frac{w_i^-}{\|w^-\| + \varepsilon} \right)}_{\text{filter normalization}} x_i + \underbrace{b}_{\text{shifting}}, \quad (13)$$

where ε is a small constant (e.g., 10^{-6}) to ensure numerical stability. This normalization step enforces the filter to become *either* averaging if w is all positive, *or* differencing if w has both positive and negative weights, ensuring atmosphere equivariance and enabling co-domain symmetry. It is then followed by learnable scaling a and shifting b , which model response weighting $\|w\|$ and offset b .

4 Experiments

Our approach normalizes convolution filters in deep networks to eliminate artifacts and enhance robustness to atmospheric perturbations. While we demonstrate its effectiveness on ResNets [13], the method is broadly applicable to any model with convolutional layers. We evaluate our approach on artificially corrupted ImageNet [9] and CIFAR [17] datasets for image classification tasks, as well as on natural data with intensity variations, including low-light and astronomy datasets. Additionally, we perform extensive analyses, ablations, and comparisons with alternative techniques such as data augmentation and normalization layers.

4.1 Results on artificially corrupted benchmarks

We use the original ImageNet-1k [9] and CIFAR-10 [17] training sets to train our models. ImageNet-1k contains over a million training images, 50K validation images, and 1,000 classes. CIFAR-10 has 10 categories, with 50K and 10K training and testing images respectively. We denote the original evaluation sets of these datasets as D .

We propose four additional evaluation sets by applying random gain and bias perturbations to D . **1)** D_C has *constant* random gain-bias corruptions to the entire image: $\tilde{x} = \mathbf{1}(\alpha x + \beta)$, where \tilde{x} is the corrupted image, and $\alpha \sim \text{Unif}(0.7, 1.3)$ and $\beta \sim \text{Unif}(-0.3, 0.3)$ are calculated to have a maximum variation of $\pm 30\%$ from the original image x intensity. **2)** D_L has gain-bias corruption in a smooth *linearly* decreasing fashion: $\tilde{x} = x \cdot \mathbf{L}_\alpha + \mathbf{L}_\beta$, where \mathbf{L}_α is a linearly varying field with values $[\alpha_0, \alpha_1]$ where $\alpha_0, \alpha_1 \sim \text{Unif}(0.5, 1.5)$ and \mathbf{L}_β a different linear field with values $[\beta_0, \beta_1]$ where $\beta_0, \beta_1 \sim \text{Unif}(-0.5, 0.5)$, both fields with the same random direction. **3)** D_B has the gain-bias perturbation in a *blob* with a fixed but decaying radius centered on a random pixel in the image: $\tilde{x} = x \cdot \mathbf{B}_\alpha + \mathbf{B}_\beta$, where \mathbf{B}_α and \mathbf{B}_β are blob fields calculated with a cubic decay over a radius of 0.8 the size of the image. D_C, D_L, D_B simulate global and local atmospheric effects such as variations in illumination caused by the environment or artificial light sources, calibration, or artifacts from sensor defects (See Fig. 2). **4)** D_S perturbation is also constant as in D_C , but with a fixed strong *shifted* bias to increase the data distribution shift: $\tilde{x} = \mathbf{1}(\alpha x + \beta + \gamma)$, where $\alpha \sim \text{Unif}(0.7, 1.3)$, $\beta \sim \text{Unif}(-0.3, 0.3)$ and $\gamma = 1$.

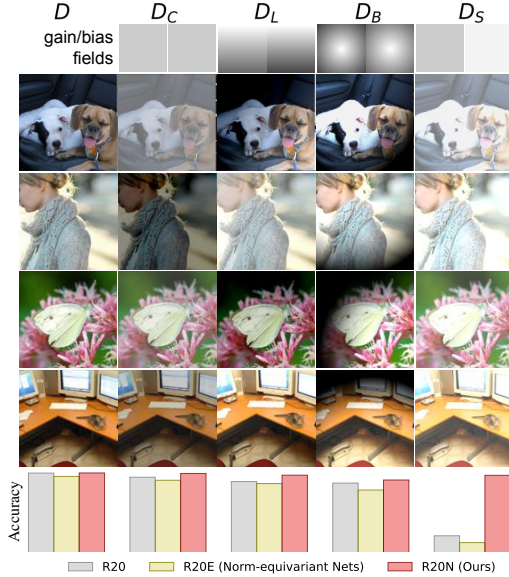


Figure 5: **Top: our corrupted evaluation benchmarks simulate realistic scenarios with varying global and local illumination sources and atmospheric effects.** We add corruptions to ImageNet original validation set (D). The first three ($D_{C,L,B}$) sets apply random atmospheres (See Fig. 2) in a constant, linear, and blob fashion. D_S applies a constant random variation with a fixed shift. **Bottom: our approach provides more robust results on the corrupted datasets and surpasses vanilla and normalization-equivariant networks across architectures while maintaining performance on the original test set.** We train vanilla (R20) and normalization-equivariant nets (R20E) [15] on the original CIFAR-10 training set and show classification accuracy on D , D_C , D_L , D_B , and D_S . Our approach (R20N) achieves a significantly lower accuracy drop compared to vanilla R20 and norm-equivariant R20E. See complete CIFAR-10 results in Appendix A.1.

We anticipate that our four corrupted evaluation sets will exhibit increasing levels of difficulty; D_C introduces a uniform perturbation across the entire image, D_L applies a linearly varying gain and bias, while D_B imposes a perturbation with a cubic decay from a randomly selected set of coordinates. On the other hand, D_S also applies a uniform corruption, but with an additional fixed bias shift, which further increases the divergence between the testing data distribution and the original training set.

Our normalized convolutions are more robust across architectures on CIFAR-10. We evaluate our proposed normalized convolutions on CIFAR with vanilla ResNets [13]. Additionally, we compare to norm-equivariant nets [15], which is the most recent baseline and closest related to our method. We replace the vanilla convolutions and activations in the ResNets with affine convolutions and sort pooling layers, respectively, from their official implementation.

We train all models using SGD with a learning rate of 0.1, a cosine annealing schedule for 200 epochs, and a batch size of 128. Fig. 5–bottom shows our approach’s superior robustness to atmospheric effects, outperforming vanilla R20 and norm-equivariant R20E. See complete results with larger models in Table A1.

To further analyze the impact of corruptions on feature representations, we visualize the last layer features on CIFAR-10’s test set using t-SNE [34]. As shown in Fig. 6–top, a vanilla R20 struggles to produce discriminative features in the presence of atmospheric variations, whereas our approach (Fig. 6–bottom) preserves features more effectively even under severe corruptions. In Appendix A.1.1 we show the performance of R20 and R20N on D_C varying the amount of corruption.

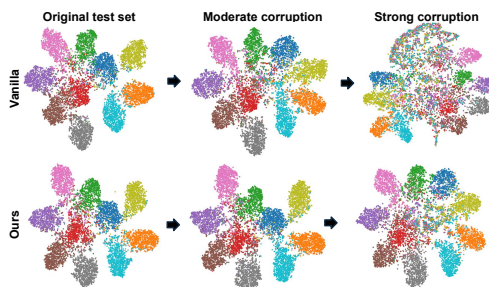


Figure 6: **Feature quality from unnormalized convolutions drops under atmospheric perturbations.** We show the t-SNE visualization of a R20 last layer’s features with moderate and strong levels of corruption on CIFAR-10. **Top:** A vanilla R20 fails under atmospheric perturbations, while **Bottom:** our approach maintains the feature quality even with strong perturbations.

Low-shot learning benefits from normalized convolutions. We investigate the benefits of our approach to other tasks. Our proposed convolutions not only produce equivariant features to gain and offset variations but also reduce the number of artifacts produced by unnormalized contrast filters. We expect these features to be particularly advantageous in low-data regimes. Table A2 shows our normalized convolutions outperforming on the original evaluation set D for very low data regimes. Additionally, Fig. 7 and Table A3 show the effectiveness of our approach on D_C , outperforming a vanilla R20 when trained with limited data. Notably, the performance gain between our approach and the baseline widens as the amount of labeled data decreases (14.4% difference with 4% data).



Figure 7: **Low-shot training benefits from normalized convolutions.** We show the accuracy on the D_C set when training with fewer labeled images (indicated by %). **Our approach** generates more robust features against atmospheric effects, while also avoiding artifacts that can occur with unnormalized convolutions.

Table 1: **Our approach surpasses vanilla CNNs and ViT-based architectures on the corrupted ImageNet-1k.** We show Top-1 accuracy on the original validation set (D) and our proposed benchmarks (D_C, D_L, D_B, D_S) for various pre-trained ResNets, ViTs, and CLIP (LAION). Our method provides more robust results on the corrupted datasets while maintaining close performance on the original set (D). Notably, R34N (22M params.) outperforms larger models like ResNet101, ViT-large, and CLIP.

Model	# par (M)	D	D_C	D_L	D_B	D_S
R34 [13]	22	73.3	68.6	64.5	36.8	2.1
R50 [13]	26	76.1	69.0	63.1	21.8	0.6
R101 [13]	45	77.4	69.1	62.9	34.0	1.1
ViT-B [10]	87	75.7	66.5	61.3	39.6	0.7
ViT-L [10]	304	79.3	72.8	67.7	41.8	1.1
CLIP-B/32 [26] [†]	151	60.2	58.4	56.4	52.3	14.3
CLIP-L/14 [26] [†]	428	68.1	67.4	66.7	65.6	49.1
R34N (ours)	22	73.2	72.8	71.7	68.1	67.0

[†]Trained on LAION-1B (Zero-shot classification accuracy)

Features from our normalized convolutions improve downstream classification on ViTs. For this set of experiments we train a small ViT [39] on CIFAR-10 with 4×4 patch size, 6 layers, 8 heads, and training hyperparameters matching those in ResNet experiments. Fig. 8 and Table A4 show that, although vulnerable to atmospheric effects, ViTs exhibit greater robustness than vanilla ResNets in this task. For instance, the small ViT achieves 80.6% accuracy on the D_S benchmark, outperforming a vanilla R44.

Next, we experiment using ResNet feature maps as input to the ViT. We use the feature maps of the last convolutional layer (16×16) as input to the ViT with the same 4×4 patch size. In Fig. 8 and Table A4 we show that using feature maps from our normalized convolutions ($R44N_f$) mitigates the impact of perturbations, outperforming the original ViT by 3.8% (84.4% vs. 80.6%) on D_S .

Our approach achieves consistent gains across CNNs and ViTs on ImageNet. We train a R34 with our normalized convolutions from scratch on the original ImageNet-1k training set for 90 epochs, a batch size of 256, and SGD with an initial learning rate of 0.1 divided by 10 every 30 epochs. In Table 1 we show that our approach (R34N) is more resilient to atmospheric corruptions, with up to 5% performance drops on our proposed benchmarks (D_C, D_L, D_B, D_S), whereas a vanilla R34 suffers significant drops of up to 97% on the most corrupted datasets. Additionally, Grad-CAM [28] visualizations in Fig. 9 show that R34 loses focus from salient regions under corruptions while our R34N produces more stable representations.

Notably, our R34N with 22M parameters achieves better results than larger models like ResNet101 (45M), ViT-B (87M), and CLIP [26] (151M) trained on much larger datasets like LAION [27].

4.2 Results on natural data

Our normalized convolutions are more robust under extreme low light conditions on ExDark dataset. We evaluate our approach on the Exclusively Dark (ExDark) Image Dataset [21], which con-

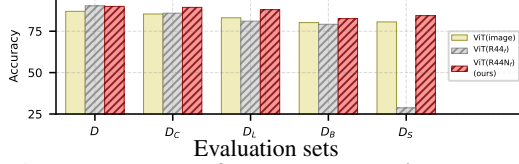


Figure 8: **Features from our normalized convolutions improve downstream classification on ViTs.** We show the accuracy of small ViTs on CIFAR-10 when trained using feature maps from a R44 as input. ViTs are more robust than vanilla ResNets, but using feature maps from **our normalized convolutions** reduces the performance drop against atmospheric effects (D_C, D_L, D_B, D_S).

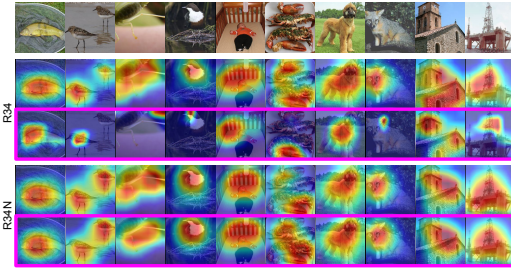


Figure 9: **Our convolutions maintain their focus on salient regions despite the presence of atmospheric effects.** Grad-CAM visualizations show that a vanilla R34 trained on ImageNet loses focus on relevant regions under corruptions (top), while our R34N produces more stable feature representations (bottom).



Figure 10: Samples from the ExDark dataset.

tains over 7,000 images captured in 10 different low-light conditions. We focus on the images labeled as “low light” (Fig. 10), to validate the robustness of our approach to extreme low-light scenes. The ExDark dataset provides image-level labels for 10 classes, which are related to ImageNet categories. Specifically, the ExDark classes are a coarser version of the ImageNet categories (e.g., ExDark has a “dog” class, while ImageNet has multiple classes for different dog species). We do a zero-shot evaluation on ExDark using a vanilla R34 and our R34N, both trained on ImageNet. We map the ImageNet labels to the coarser ExDark labels and evaluate the models. Our R34N achieves 34.2% classification accuracy, outperforming R34 (28.3%).

Our normalized convolutions generalize better across galaxies in astronomy data from LEGUS. Star cluster classification from galaxies is an active research area in astrophysics, as it provides insights into the process of star formation [12, 1]. As new telescopes like the James Webb (JWST) continue to capture new data, models that can generalize across galaxies becomes increasingly important.

We explore the potential of our normalized convolutions using the LEGUS dataset [3], which contains data from 34 galaxies captured by the Hubble telescope (HST) with 5 spectral channels and $\sim 15,000$ annotated star clusters and other sources. We evaluate the robustness to varying luminance conditions by training and evaluating on different targets. Specifically, we use galaxies NGC628 and NGC1313 which have a noticeable difference in intensity (Fig. 11a).

We train a R18 on NGC628 using around 2,000 object-centered patches of size $32 \times 32 \times 5$ from coordinates provided in LEGUS (See Fig. 11b), to classify them into one of four morphological classes.

We use training hyperparameters as in [25] and evaluate on galaxy NGC1313 sources. Our results show an accuracy of 50.2% with vanilla R18, while our R18N improves accuracy to 51.9%.

4.3 Analysis and ablation studies

Unnormalized filters learn less diverse representations. Normalization can promote diversity by forcing the filters to lie on a specific manifold. We study filter similarity using guided backpropagation [31] to visualize filter gradients with respect to the images on the ImageNet validation set. Then, we compute the correlation matrix of the guided backpropagation maps of each filter in a layer and plot the histogram of its off-diagonal elements. Low values from the off-diagonal elements indicate less similar features.

Fig. 12 shows that our R34N learns less correlated features, with a histogram more skewed towards zero.

Unnormalized filters produce more errors. We investigate the relationship between a filter’s level of “unnormalization” and misclassifications. First, we sort the filters in the first layer of an ImageNet pretrained R34 based on the absolute value of their positive weight ratio ($|r(w)|$). We expect this metric to be 0 for normalized differencing filters (See Fig. 13–left). Then, focusing on the first layer, where gain and bias effects are largest, we find the Top 100 images on D_C that maximize the response for each filter and calculate the number of misclassified ones by the network.

In Fig. 13–right we show that for a R34, the images with a higher response from filters with higher $|r(w)|$ are more likely to be misclassified. For instance, filters with highest $|r(w)|$ misclassify $\sim 67\%$ of the images, while the least unnormalized misclassify $\sim 30\%$. Our R34N avoid this issue by design.

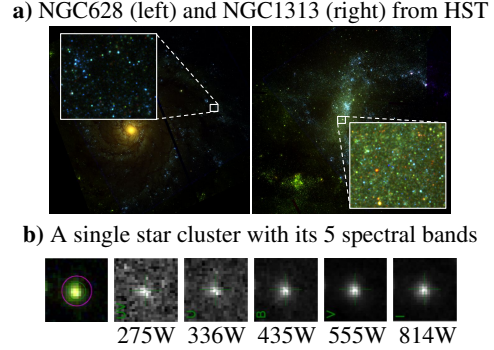


Figure 11: **Astronomy data suffers from significant intensity variations, similar to atmospheric effects on standard photographs.** **a)** Galaxies NGC628 (left) and NGC1313 (right) from HST data, showing higher luminance in NGC1313 due to background light caused by dust and gas. **b)** A star cluster crop with its five spectral bands (275W-814W) from the LEGUS dataset.

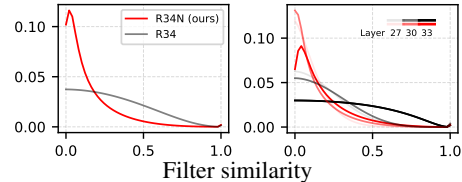


Figure 12: **Unnormalized filters produce less diverse features.** We compare the filter similarity histograms of a vanilla R34 and our R34N trained on ImageNet. **Left:** The histogram for the last eight convolutional layers shows that R34N has a more skewed distribution towards lower similarity values than vanilla R34. **Right:** Consistent with [35], layer-wise histograms reveal that vanilla R34 produces more similar features in later layers, whereas R34N does not exhibit this trend.

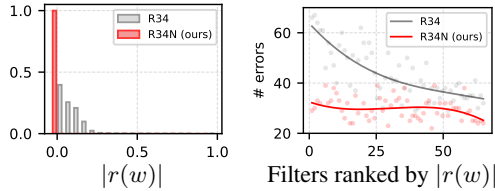


Figure 13: **Unnormalized filters misclassify more often.** We investigate how filter weight normalization affects error rates in a pretrained R34. **Left:** We show the histogram of $|r(w)|$ from all filter weights in the network. We want this ratio to be 0 if the filters are differencing, or 1 if they are averaging filters. The peak in 0 from our R34N indicates all our filters are differencing and normalized, while vanilla ResNets possess many unnormalized. **Right:** We sort filters by “unnormalization” level and find that images triggering strong responses from “less normalized” filters (i.e., higher $|r(w)|$) are more often misclassified. Our convolutions avoid this by design.

Are data augmentations enough? To evaluate the effectiveness of data augmentation, we train a vanilla R20 and our proposed R20N using atmospheric augmentations on CIFAR-10. We use random gain-bias augmentations with a maximum variation of $\pm 10\%$ from the original image intensity to simulate the case where we want to approximate the testing data distribution but we do not know the *exact* distribution (e.g., $\pm 30\%$ maximum variation on D_C).

Our results in Table 2 show that data augmentation provides significant robustness, even with lower gain-bias variation than the test set. However, when data distributions differ substantially, as in D_S , data augmentation falls short, with our R20N achieving 91% accuracy vs. 77% from R20.

Table 2: **Training with data augmentations helps but struggles with significantly different data distributions.** We train a R20 with and without gain-bias augmentations and evaluate on our proposed benchmarks. **Left:** Without needing gain-bias augmentations, our R20N beats vanilla R20 in all corrupted datasets. **Right:** While using augmentations improves accuracy across all benchmarks for vanilla R20, it struggles to generalize to significantly different data distributions, such as D_S .

Without data augmentations						With data augmentations					
Model	D	D_C	D_L	D_B	D_S	Model	D	D_C	D_L	D_B	D_S
R20	91.4	87.9	84.2	82.9	38.1	R20	91.9	91.6	90.8	88.0	76.9
R20N (ours)	91.5	91.1	89.6	85.5	89.5	R20N (ours)	91.9	91.7	90.8	87.1	90.8

Comparison to instance normalization (IN). IN reduces instance-specific biases, improving robustness against atmospheric variations as shown in Fig. 14. In contrast, a R20 with BN suffers significant accuracy drops ($\sim 60\%$). However, IN may not fully address covariate shift, leading to suboptimal training (89.0% vs. 91.4% accuracy on the original set with R20+BN). BN stabilizes training by addressing internal covariate shift but does not improve codomain symmetry like IN and our approach. Our method lets us use BN while taking care of the atmospheric effects, achieving improved performance on most benchmarks while maintaining accuracy on D .

While both IN and our approach mitigate instance-specific biases, ours offers two key distinctions: 1) independent normalization of weights, which reduces artifacts; and 2) normalization of weights rather than activations, providing a more targeted correction.

Negligible computational overhead. Filter normalization’s potential expressivity loss is addressed by learnable scale and shift parameters, adding only 0.08% parameters to an R34. Notably, this increase is unnecessary with batch normalization since these parameters are learned in the batchnorm layers. Our approach also incurs almost no inference-time overhead; only a +0.06 ms per image increase for R34, when measured on ImageNet’s validation set using an RTX 2080 Ti.

Summary. We identify unnormalized filters as a key deep learning limitation and propose filter normalization, ensuring atmospheric equivariance. We achieve consistent gains across CNNs and ViTs, outperforming larger models like CLIP, while enhancing robustness and generalization. Our code will be publicly available upon publication.

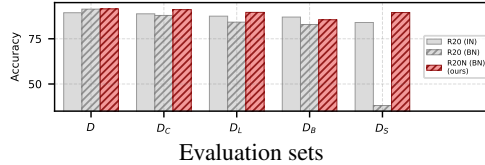


Figure 14: **Instance normalization improves robustness to atmospheric effects but may not fully address covariate shift, leading to suboptimal training.** We compare a vanilla R44 trained on CIFAR-10 with instance normalization layers to a vanilla R44 with batch normalization and our R44N. We get best results on most benchmarks while maintaining original test set accuracy (D). Our approach differs from instance norm. in two ways: independent normalization of positive and negative weights, reducing artifacts; and normalizing weights, not activations.

References

- [1] A. Adamo, G. Östlin, and E. Zackrisson. Probing cluster formation under extreme conditions: massive star clusters in blue compact galaxies. *Monthly Notices of the Royal Astronomical Society*, 417(3):1904–1912, 10 2011.
- [2] E. H. Adelson. Lightness perception and lightness illusions. 1999.
- [3] D. Calzetti, J. Lee, E. Sabbi, and A. Adamo. Legacy extragalactic uv survey (legus) with the hubble space telescope. i. survey description. *The Astronomical Journal*, 149(51):25, 2015.
- [4] R. Chakraborty, Y. Xing, and S. X. Yu. Surreal: Complex-valued learning as principled transformations on a scaling and rotation manifold. *IEEE Transactions on Neural Networks and Learning Systems*, 33(3):940–951, 2022.
- [5] T. S. Cohen and M. Welling. Steerable CNNs. In *International Conference on Learning Representations (ICLR)*, 2017.
- [6] M. Cotogni and C. Cusano. Offset equivariant networks and their applications. *Neurocomputing*, 502:110–119, 2022.
- [7] E. D. Cubuk, B. Zoph, D. Mané, V. Vasudevan, and Q. V. Le. Autoaugment: Learning augmentation strategies from data. In *IEEE/CVF Conference on Computer Vision and Pattern Recognition (CVPR)*, pages 113–123. Computer Vision Foundation / IEEE, 2019.
- [8] E. D. Cubuk, B. Zoph, J. Shlens, and Q. Le. Randaugment: Practical automated data augmentation with a reduced search space. In H. Larochelle, M. Ranzato, R. Hadsell, M. Balcan, and H. Lin, editors, *Advances in Neural Information Processing Systems (NeurIPS)*, volume 33, pages 18613–18624. Curran Associates, Inc., 2020.
- [9] J. Deng, W. Dong, R. Socher, L.-J. Li, K. Li, and L. Fei-Fei. ImageNet: A large-scale hierarchical image database. In *IEEE/CVF Conference on Computer Vision and Pattern Recognition (CVPR)*, 2009.
- [10] A. Dosovitskiy, L. Beyer, A. Kolesnikov, D. Weissenborn, X. Zhai, T. Unterthiner, M. Dehghani, M. Minderer, G. Heigold, S. Gelly, J. Uszkoreit, and N. Houlsby. An image is worth 16x16 words: Transformers for image recognition at scale. *International Conference on Learning Representations (ICLR)*, 2021.
- [11] C. Esteves, C. Allen-Blanchette, X. Zhou, and K. Daniilidis. Polar transformer networks. In *International Conference on Learning Representations (ICLR)*, 2018.
- [12] K. Glatt, E. K. Grebel, and A. Koch. Ages and Luminosities of Young SMC/LMC Star Clusters and the recent Star Formation History of the Clouds. *Astron. Astrophys.*, 517:A50, 2010.
- [13] K. He, X. Zhang, S. Ren, and J. Sun. Deep residual learning for image recognition. In *IEEE/CVF Conference on Computer Vision and Pattern Recognition (CVPR)*, 2016.
- [14] D. Hendrycks and T. Dietterich. Benchmarking neural network robustness to common corruptions and perturbations. *Proceedings of the International Conference on Learning Representations*, 2019.
- [15] S. Herbreteau, E. Moebel, and C. Kervrann. Normalization-equivariant neural networks with application to image denoising. In *Advances in Neural Information Processing Systems (NeurIPS)*, volume 36, pages 5706–5728, 2023.
- [16] S. Ioffe and C. Szegedy. Batch normalization: Accelerating deep network training by reducing internal covariate shift. *CoRR*, abs/1502.03167, 2015.
- [17] A. Krizhevsky. Learning multiple layers of features from tiny images. pages 32–33, 2009.
- [18] Y. LeCun, B. Boser, J. S. Denker, D. Henderson, R. E. Howard, W. Hubbard, and L. D. Jackel. Backpropagation applied to handwritten zip code recognition. *Neural computation*, 1(4):541–551, 1989.
- [19] J. Li, Z. Yang, H. Liu, and D. Cai. Deep rotation equivariant network. *Neurocomput.*, 290(C):26–33, May 2018.
- [20] Z. Liu, H. Mao, C.-Y. Wu, C. Feichtenhofer, T. Darrell, and S. Xie. A convnet for the 2020s. *IEEE/CVF Conference on Computer Vision and Pattern Recognition (CVPR)*, 2022.
- [21] Y. P. Loh and C. S. Chan. Getting to know low-light images with the exclusively dark dataset. *Computer Vision and Image Understanding*, 178:30–42, 2019.

- [22] H. Mo and G. Zhao. Ric-cnn: Rotation-invariant coordinate convolutional neural network. *Pattern Recogn.*, 146(C), Feb. 2024.
- [23] S. Mohan, Z. Kadkhodaie, E. P. Simoncelli, and C. Fernandez-Granda. Robust and interpretable blind image denoising via bias-free convolutional neural networks. In *International Conference on Learning Representations (ICLR)*, 2020.
- [24] C. Olah, A. Mordvintsev, and L. Schubert. Feature visualization. *Distill*, 2(11):e7, 2017.
- [25] G. Perez, M. Messa, D. Calzetti, S. Maji, D. E. Jung, A. Adamo, and M. Sirressi. StarcNet: Machine learning for star cluster identification. *The Astrophysical Journal*, 907(2):100, feb 2021.
- [26] A. Radford, J. W. Kim, C. Hallacy, A. Ramesh, G. Goh, S. Agarwal, G. Sastry, A. Askell, P. Mishkin, J. Clark, G. Krueger, and I. Sutskever. Learning transferable visual models from natural language supervision. In M. Meila and T. Zhang, editors, *Proceedings of the 38th International Conference on Machine Learning*, volume 139 of *Proceedings of Machine Learning Research*, pages 8748–8763. PMLR, 18–24 Jul 2021.
- [27] C. Schuhmann, R. Beaumont, R. Vencu, C. W. Gordon, R. Wightman, M. Cherti, T. Coombes, A. Katta, C. Mullis, M. Wortsman, P. Schramowski, S. R. Kundurthy, K. Crowson, L. Schmidt, R. Kaczmarczyk, and J. Jitsev. LAION-5b: An open large-scale dataset for training next generation image-text models. In *Thirty-sixth Conference on Neural Information Processing Systems Datasets and Benchmarks Track*, 2022.
- [28] R. R. Selvaraju, M. Cogswell, A. Das, R. Vedantam, D. Parikh, and D. Batra. Grad-cam: Visual explanations from deep networks via gradient-based localization. In *IEEE International Conference on Computer Vision (ICCV)*, pages 618–626, 2017.
- [29] K. Simonyan, A. Vedaldi, and A. Zisserman. Deep inside convolutional networks: Visualising image classification models and saliency maps. *arXiv preprint arXiv:1312.6034*, 2013.
- [30] U. Singhal, Y. Xing, and S. X. Yu. Co-domain symmetry for complex-valued deep learning. In *IEEE/CVF Conference on Computer Vision and Pattern Recognition (CVPR)*, pages 681–690, June 2022.
- [31] J. T. Springenberg, A. Dosovitskiy, T. Brox, and M. A. Riedmiller. Striving for simplicity: The all convolutional net. In *International Conference on Learning Representations (ICLR)*, 2015.
- [32] N. Srivastava, E. Mansimov, and R. Salakhudinov. Unsupervised learning of video representations using lstms. *arXiv preprint arXiv:1502.04681*, 2015.
- [33] D. Ulyanov, A. Vedaldi, and V. S. Lempitsky. Instance normalization: The missing ingredient for fast stylization. *ArXiv*, abs/1607.08022, 2016.
- [34] L. van der Maaten and G. Hinton. Visualizing data using t-SNE. *Journal of Machine Learning Research*, 9:2579–2605, 2008.
- [35] X. Wang and S. X. Yu. Tied block convolution: Leaner and better cnns with shared thinner filters. *Proceedings of the AAAI Conference on Artificial Intelligence*, 35:10227–10235, May 2021.
- [36] D. E. Worrall, S. J. Garbin, D. Turmukhambetov, and G. J. Brostow. Harmonic Networks: Deep Translation and Rotation Equivariance. In *IEEE/CVF Conference on Computer Vision and Pattern Recognition (CVPR)*, pages 7168–7177. IEEE Computer Society, July 2017.
- [37] H. Wu, B. Xiao, N. Codella, M. Liu, X. Dai, L. Yuan, and L. Zhang. Cvt: Introducing convolutions to vision transformers. *arXiv preprint arXiv:2103.15808*, 2021.
- [38] Y. Wu and K. He. Group normalization. In *Proceedings of the European Conference on Computer Vision (ECCV)*, September 2018.
- [39] K. Yoshioka. vision-transformers-cifar10: Training vision transformers (vit) and related models on cifar-10. <https://github.com/kentaroy47/vision-transformers-cifar10>, 2024.
- [40] J. Yosinski, J. Clune, A. Nguyen, T. Fuchs, and H. Lipson. Understanding neural networks through deep visualization. *arXiv preprint arXiv:1506.06579*, 2015.
- [41] M. D. Zeiler and R. Fergus. Visualizing and understanding convolutional networks. *European conference on computer vision*, pages 818–833, 2014.

Supplementary material

A Supporting experiments

The supplementary material provides more comprehensive tables with results from our main experiments and ablations on CIFAR-10 in § 4. Specifically, tables providing numerical results from Figures 5, 7, 8, and 14 in § A.1, A.2, A.3, and A.4. We also provide an ablation with an increasing amount of corruption in § A.1.1, and analysis on enforcing normalization as a soft regularization in contrast to our method in § A.5. Additionally, we include the training curves of the vanilla R34 and our R34N trained on ImageNet-1k in § A.6 and learned filter visualizations in § A.7.

A.1 Classification on CIFAR-10

Table A1: **Accuracy on CIFAR-10.** We train the models on the original training sets and evaluate them on the original test set (D) and our proposed benchmarks ($D_{C,L,B,S}$). Our method provides more robust results with all models on the corrupted datasets while maintaining the same performance on the original test set.

	Model (vanilla [13] / norm-equiv [15] / ours)								
	R20	R20E	R20N	R32	R32E	R32N	R44	R44E	R44N
D	91.4	88.6	91.5	92.0	89.7	92.0	93.2	89.0	93.2
D_C	87.9	85.3	91.1	87.7	86.5	91.5	89.7	86.7	92.6
D_L	84.2	82.5	89.6	84.3	84.0	90.4	86.4	83.6	92.0
D_B	82.9	77.0	85.5	80.1	76.2	87.6	87.3	80.6	87.8
D_S	38.1	32.3	89.5	28.6	27.8	88.8	49.5	52.2	90.2

A.1.1 Ablation with increasing corruption

Here we show the accuracy of a vanilla R20 and our proposed R20N evaluated on the corrupted CIFAR-10 evaluation set D_C with varying amounts of corruption. In Fig. A1 we can see that our R20N is more robust to increasing amounts of gain and bias perturbations.

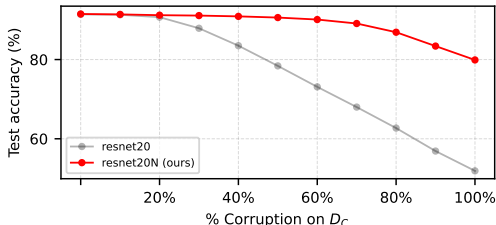


Figure A1: **Our normalized convolutions are more robust to increasing levels of corruption.** A vanilla R20 and our proposed R20N trained on the original CIFAR-10 training set and evaluated on the corrupted evaluation set D_C with increasing levels of gain and bias corruption.

A.2 Low-shot learning

Table A2 shows our normalized convolutions outperforming on the original evaluation set D for very low data regimes. In Table. A3 we show results for low-show training experiments. Our approach suffers less from reduced training data. Notably, the performance gap between our approach and the baseline widens as the amount of labeled data decreases. See § 4.1 for more details.

Table A2: **Low-shot training results on D .** Accuracy on the D evaluation set in very low data regimes (indicated by %). Our approach suffers less from reduced training data.

% train data	1%	2%	4%	6%	8%	10%
R20	41.4	51.0	61.6	68.0	74.0	75.4
R20N (ours)	46.3	55.8	67.0	69.9	75.0	75.6

Table A3: **Low-shot training results on D_C** . Accuracy on the D_C evaluation set when training with fewer labeled images (indicated by %). Our approach suffers less from reduced training data. Notably, the performance gap between our approach and the baseline widens as the amount of labeled data decreases (bottom row).

% train data	4%	6%	8%	10%	20%	40%	60%	80%
R20	51.5	60.2	68.6	68.8	78.0	82.4	85.6	87.4
R20N (ours)	65.9	69.2	74.1	74.2	81.7	85.8	88.6	89.3
Gain	+14.4	+9.0	+5.5	+5.4	+3.7	+3.4	+3.0	+1.9

A.3 Downstream classification with ViTs

In Table. A4 we show our experiments on downstream classification with ViTs using R20, R32, and R44 features as input. We compare to our features using normalized convolutions. See § 4.1 for more details.

Table A4: **Downstream classification on ViTs**. We evaluate the performance of a small ViT [39] on CIFAR-10 on our proposed benchmarks using the raw image as input (left column) and feature maps from ResNets. ViT exhibits more robustness than vanilla ResNets (Table A1), but using feature maps from our normalized convolutions significantly reduces the performance drop after perturbations compared to all the other baselines.

	Image (J) $\in \mathbb{R}^{32 \times 32}$	ViT [39] input type					
		ResNet feature maps ($f \in \mathbb{R}^{16 \times 16}$)					
		R20 _f	R20N _f	R32 _f	R32N _f	R44 _f	R44N _f
D_C	85.4	86.4	88.8	84.7	88.5	85.9	89.4
D_L	83.1	82.4	87.2	80.4	87.6	81.1	88.0
D_B	80.2	79.2	80.2	77.6	81.9	79.2	82.6
D_S	<u>80.6</u>	39.9	84.4	32.6	84.7	28.7	84.4

A.4 Comparison to normalization layers

In Table. A5 we present the results with different normalization layers for R20, R32, and R44 on CIFAR-10. Specifically, we show results with instance normalization (IN), batch normalization (BN), and without any normalization layer (\times), where we get the best results on most benchmarks while maintaining original test set accuracy. See § 4.3 for more details.

Table A5: **Ablation with normalization layers**. We train ResNets on CIFAR-10 with different normalization layers using vanilla convolutions and our normalized convolutions. We get best results on most benchmarks while maintaining original test set accuracy.

	ResNet20			ResNet20N (ours)			ResNet32			ResNet32N (ours)			ResNet44			ResNet44N (ours)		
	\times	IN	BN	\times	IN	BN	\times	IN	BN	\times	IN	BN	\times	IN	BN	\times	IN	BN
D	89.0	89.4	91.4	88.1	90.1	91.5	88.8	90.0	92.0	89.6	90.7	92.0	89.2	90.5	93.2	90.4	90.7	93.2
D_C	86.2	88.8	87.9	87.5	89.7	91.1	85.8	90.0	87.7	88.9	90.2	91.5	86.6	90.3	89.7	89.5	90.4	92.6
D_L	83.8	87.5	84.2	86.3	88.8	89.6	82.7	88.4	84.3	87.9	89.1	90.4	82.7	89.2	86.4	88.3	89.9	92.0
D_B	80.7	87.0	82.9	81.6	87.6	85.5	80.8	88.2	80.1	83.1	88.1	87.6	81.5	88.8	87.3	83.6	88.5	87.8
D_S	43.5	84.0	38.1	85.9	79.4	89.5	42.9	88.1	28.6	85.9	79.2	88.8	43.2	89.3	49.5	86.9	85.4	90.2

A.5 Normalization as soft regularization

We compare our approach to weight normalization through soft regularization. Specifically, given the set of convolutional filter weights W in a CNN, where each filter weight is a 3D tensor $w \in \mathbb{R}^{C \times M \times N}$, the regularization term is given by

$$R(W) = \sum_{w \in W} \left(|1 - \|w^+\|| + |1 - \|w^-\|| \right). \quad (14)$$

The total loss function with regularization can be written as $L_{total} = L + \alpha R(W)$, where $\alpha = 0.01$ controls the strength of the regularization. We add this regularization to the loss during training of a R20 on CIFAR-10 using the same hyperparameters from § 4.1. In Table A6 we show that

regularization improves robustness over vanilla training (second row), but our approach yields significantly better results (bottom row). While regularization may reduce $|r(w)|$ it does not guarantee $|r(w)| = 0$ for all filters like our approach (Fig. 13).

Table A6: **Our normalized convolutions beat normalization as soft regularization.** Adding the soft regularization (\checkmark) improves the robustness of vanilla R20 (see first two rows), but our approach surpasses soft regularization (see the two bottom rows). Underlined values show the best accuracy against their non-regularized counterpart, while **bold** values show the best overall.

Model	soft reg.	D	D_C	D_L	D_B	D_S
R20		91.4	87.9	84.2	82.9	38.1
R20	\checkmark	92.0	88.8	85.9	84.1	48.8
R20N		91.5	91.1	89.6	85.5	89.5
R20N	\checkmark	92.0	91.5	90.5	86.0	89.0

A.6 R34 training curves on ImageNet

Here we show the training curves of the vanilla R34 and our R34N on ImageNet-1k. We train both networks from scratch on the original ImageNet-1k training set for 90 epochs, a batch size of 256, and SGD with an initial learning rate of 0.1 divided by 10 every 30 epochs. In Fig. A2 we can see that our R34N exhibits a more stable validation accuracy throughout training.

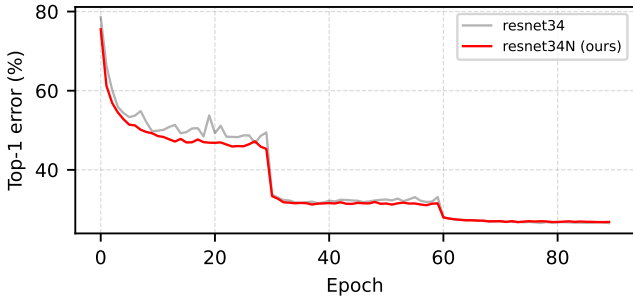


Figure A2: **Filter normalization regularizes learning showing more stable validation accuracy during training.** ResNet34 training curve on ImageNet-1k with the hyperparameters described in the ImageNet experiments in § 4.1.

A.7 Feature visualizations

In Fig. A3 we show the learned filters from the first layer of R34 (left) and our R34N (right) models, trained on ImageNet-1k using the hyperparameters in § 4.1. Our model with normalized convolutions (R34N) exhibits more diverse features, consistent with the results in Fig. 12.

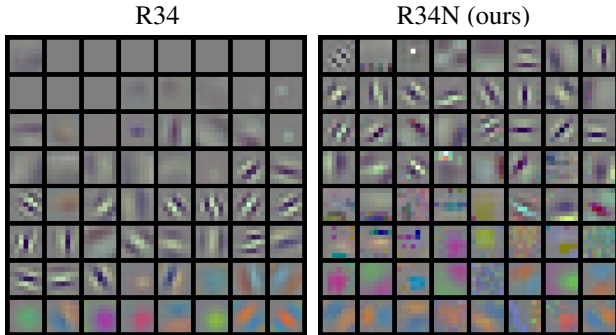


Figure A3: **Filter visualizations.** Learned filters from the first layer of R34 (left) and R34N (right) models, trained on ImageNet-1k. Our R34N exhibits more diverse features.

A.8 Results on ImageNet-C and ImageNet-P

We train a R34 and our R34N on the clean ImageNet-1k training set and evaluate them on the ImageNet-C and ImageNet-P datasets [14]. ImageNet-C tests model robustness by applying various corruptions to images, while ImageNet-P evaluates model stability by applying 30 levels of increasing perturbations and measuring the Flip Rate (FR), which is the frequency of changed predictions from the original image’s predicted class. For ImageNet-C, we assess performance across all corruption levels, and for ImageNet-P, we assess performance at the maximum perturbation level. We evaluate the weather and noise corruption groups for both datasets, as they are the most relevant for this work.

In Table A7, we observe comparable results, which we attribute to the clipping of ImageNet-C and ImageNet-P images are saved to disk. This clipping likely causes information loss, particularly under extreme corruptions like high gain or bias, resulting in overexposed regions with saturated pixel values (e.g., pure white). Unlike scientific imaging formats like FITS, which preserve dynamic range, the clipped images may limit the effectiveness of our approach.

Table A7: **Results on ImageNet-C and ImageNet-P.** We show the Top-1 accuracy (Acc. \uparrow) for ImageNet-C and the Flip Rate (FR \downarrow) for ImageNet-P, focusing on weather and noise corruption groups. We observe comparable results, likely due to clipping that occurs when ImageNet-C and ImageNet-P images are saved to disk.

Model	ImageNet-C (Acc. \uparrow)		ImageNet-P (FR \downarrow)	
	Weather	Noise	Weather	Noise
R34	41.6	27.4	41.3	23.5
R34N	41.0	28.1	40.0	24.9